

# Aerothermal comparison of a diffuser hole and a slot geometry: Thermal performance and jet stability

## Original article

### Article history:

Submission date: 6 October 2022

Acceptance date: 5 April 2023

Publication date: 10 July 2023

This is the updated version of a paper originally presented at the Global Power and Propulsion Technical Conference, GPPS Chania22, September 11–14, 2022.



### \*Correspondence:

KS: katharina.stichling@kit.edu

### Peer review:

Single blind

### Copyright:

© 2023 Stichling and Bauer © This is an open access article distributed under the Creative Commons Attribution License (CC-BY 4.0), which permits unrestricted use, distribution, and reproduction in any medium, provided the original work is properly cited and its authors credited.

### Keywords:

film cooling; heat transfer; coherent structures; stereoscopic particle image velocimetry; infrared thermography

### Citation:

Stichling K., Bauer H.-J. (2023). Aerothermal comparison of a diffuser hole and a slot geometry: Thermal performance and jet stability. *Journal of the Global Power and Propulsion Society*. 7: 211–221. <https://doi.org/10.33737/jgpps/163087>

Katharina Stichling<sup>1\*</sup>, Hans-Jörg Bauer<sup>1</sup>

<sup>1</sup>Karlsruhe Institute of Technology, Straße am Forum 6, 76131 Karlsruhe, Baden-Württemberg, Germany

## Abstract

Numerous experimental investigations, predominantly determining the adiabatic film cooling effectiveness and the heat transfer coefficient with film cooling dependent on parameters such as blowing ratio ( $M$ ), density ratio ( $DR$ ), velocity ratio ( $VR$ ) and momentum flux ratio ( $IR$ ) have been conducted in the past for a vast variety of geometries. To fully characterize a jet in cross-flow for its application in film cooling, thermal and aerodynamic parameters have to be analysed in conjunction.

In the present work, detailed flow field measurements using Stereoscopic Particle Image Velocimetry (SPIV) are conducted at engine-realistic operating conditions in a test rig at the Institute of Thermal Turbomachinery (ITS) at the Karlsruhe Institute of Technology (KIT). Additionally, thermal measurements using Infrared Thermography (IRT) are carried out to determine the adiabatic film cooling effectiveness and the heat transfer coefficient with film cooling. Two film cooling hole geometries are analysed: A  $10^\circ$ - $10^\circ$ - $10^\circ$  laidback fan-shaped shaped film cooling hole (LFH10) and a slot geometry with a plenum-like inlet. Flow field data, and thermal film cooling quantities are analysed to quantify and characterize their aero-thermal behaviour. The significance of the stability and continuity of the exiting film cooling jets for the thermal performance is demonstrated to comprehend the differences in how efficiently the provided cooling air is used. It is shown that the absence of the counter-rotating vortex pair may not necessarily lead to an improved adiabatic film cooling effectiveness  $\eta_{a,w}$ .

## Introduction

An increasing demand for more sustainable gas turbines and aero engines requires increasing efficiencies (Krein and Williams, 2012). Higher efficiencies can be achieved by further increasing the pressure ratio and turbine entry temperature (TET). To facilitate a higher TET, the cooling methods and more specifically film cooling has to be further improved. This requires a thorough understanding of the interaction between coolant jet and hot gas. It will enable the development of more efficient thus sustainable gas turbines and aero-engines.

Numerous experimental investigations, predominantly determining thermal film cooling quantities such as adiabatic film cooling effectiveness and ratio of heat transfer coefficients with and without film cooling dependent on various parameters such as blowing ratio ( $BR = (\rho u)_c / (\rho u)_h$ ), density ratio ( $DR = \rho_c / \rho_h$ ), velocity ratio ( $VR = (u)_c / (u)_h$ ) or momentum ratio ( $IR = (\rho u^2)_c / (\rho u^2)_h$ ) have been conducted in the past. Investigations retaining all relevant dimensionless parameters while also considering coolant cross-flow and coolant cross-flow direction are rare and to the authors best knowledge only conducted by Fraas et al. (2019a,b) for a

laidback fan-shaped and optimised cooling hole geometries, respectively. Aside from an overall wide range of available thermal film cooling measurement data (for reference on shaped holes see [Bunker \(2005\)](#)), flow field measurements in combination with thermal measurements optimally from the same experimental facility are required to fully understand all effects observed in thermal film cooling quantities.

[Hale et al. \(2000\)](#) investigated  $90^\circ$  jets in cross-flow considering parallel and reversed parallel coolant cross-flow. They used flow visualisation, surface heat transfer measurements and numerical simulations to relate flow field and heat transfer, but the operating conditions do not replicate density ratio, free stream turbulence or length scales as they are expected in gas turbines or aero engines. [Aga \(2009\)](#) analysed the influence of flow structures on film cooling parameters for compound angled holes but neglect coolant cross-flow, turbulence intensity and temperature ratio, instead using foreign gas to replicate engine-realistic density ratios. Joint studies of the flow field and thermal film cooling quantities were conducted investigating the effect of freestream turbulence intensity on film cooling ejection at low blowing ratios for cylindrical and fan-shaped holes ([Wright et al., 2011a,b](#); [Johnson et al., 2014](#)). Unfortunately, only unity density ratio has been used in their studies which prevents a direct application to realistic engine-like conditions. A good qualitative agreement but large local quantitative differences were observed when comparing flow field and thermal measurement data to numerical simulations ([auf dem Kampe et al., 2012](#)). The effect of high free stream turbulence on the flow field was further investigated in [Schroeder and Thole \(2016\)](#), but also neglecting coolant cross-flow.

None of the previously mentioned studies consider coolant cross-flow as well as engine-realistic density ratios and turbulence intensities. Engine-realistic operating conditions are, however, extremely relevant to achieve meaningful insights into the cooling performance and flow field in the regime of hot gas coolant interaction. Therefore, conjoint investigations combining flow field information and thermal film cooling quantities are required considering all relevant dimensionless parameters. Aside from mean flow quantities, the present study shows that the instantaneous flow field is relevant for fully understanding the time-averaged flow fields and thermal film cooling parameters.

## Methodology

In this section, the test facility is outlined. Furthermore, the measurement setup and the measurement principles are provided and the uncertainties are discussed.

## Test section and measurement setup

The schematic setup of the test section and measurement setup used for the current investigation is displayed in [Figure 1](#). The test section in [Figure 1a](#) was constructed for acquisition of adiabatic film cooling effectiveness

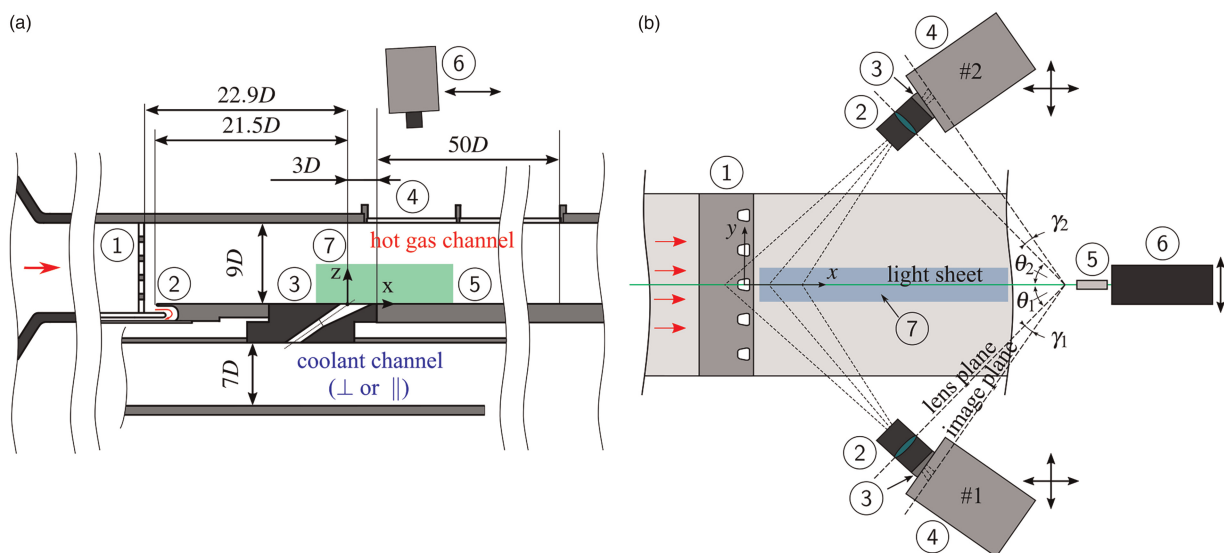


Figure 1. Schematics of test section and measurement setup including FOVs for IRT and SPIV measurements. (a) Schematic of test section containing hot gas and coolant channel including a turbulence grid ①, boundary layer suction ②, ejection module ③, optical access for IRT ④, thermal measurement plate ⑤, IRT camera ⑥ and FOV for SPIV ⑦; adapted from ([Fraas et al., 2017](#)). (b) Schematic SPIV Setup as top view on test section including: ejection module ①, camera lens ②, Scheimpflug adapter ③, camera ④, light sheet optics ⑤, ND:YLF laser ⑥ and FOV for IRT ⑦; adapted from ([Stichling et al., 2021](#)).

$\eta_{a,W}(=T_{rec,h}-T_{aw}/T_{rec,h}-T_{t,c})$  and ratio of heat transfer coefficients with and without film cooling  $h_f/b_0$  on a flat plate. Uniformity of the inlet hot gas flow in terms of velocity and temperature field have been validated in previous works (Fraas et al., 2017). The test section consists of a hot gas and a coolant channel, where the latter can be oriented either in parallel or perpendicular to the hot gas channel, therefore facilitating realistic inflow conditions present in gas turbines and aero engines. The operating conditions for this study were derived from real-engine conditions and are summarised in Table 1 (Fraas et al., 2017).

A turbulence grid (Roach, 1987) is placed downstream of the inlet nozzle ① and in combination with a subsequent boundary layer bleed ② is used to ensure well-defined and engine-like flow conditions at the coolant ejection. Coolant and hot gas channel are connected via the interchangeable ejection module ③ containing three to five separate film cooling holes aligned laterally at a constant  $x/D$ -position. To prevent interaction between coolant jet and channel sidewalls a  $50D$  wide hot gas channel is used. The ejection module is manufactured from polyetheretherketone (PEEK), a semi-crystalline high-temperature resistant thermoplastic with a low thermal conductivity of  $\lambda_{th} \approx 0.27 \text{ W/(mK)}$ . The temperature change of the coolant during ejection is thus minimized. Five infrared-transmissive sapphire windows ④ provide optical access through the top wall of the hot gas channel for temperature field acquisition on the thermal measurement plates ⑤ using a camera sensitive for infrared radiation between  $3 \dots 5 \mu\text{m}$  ⑥. For temperature calibration, a routine developed at ITS (Ochs et al., 2009) was used including adaptations for high dynamic range temperature data (Ochs et al., 2010). For calculating the thermal film cooling quantities, the superposition principle of film cooling (Choe et al. 1974) was used. Details regarding the test setup including the two thermal measurement plates and the calculation of the film cooling quantities can be found in Fraas et al. (2017).

The test section was adapted to accommodate stereoscopic Particle Image Velocimetry Measurements (SPIV) (Stichling et al., 2021) capturing the field of view (FOV) ⑦ indicated by the green area in Figure 1a. The SPIV measurement setup is detailed in Figure 1b using a top view on the hot gas channel of the test section from Figure 1a. Optical access for the SPIV measurement is granted via two fused silica windows (not displayed), one on each lateral wall of the hot gas channel. A light sheet with a thickness of  $\delta_z \approx 1.5 \text{ mm}$  is produced via the light sheet optics ⑧ using a green ( $\lambda = 527 \text{ nm}$ ) dual pulse ND:YLF laser ⑨ (Darwin-Duo by Quantronix). It is placed such that streamwise, wall-normal measurement planes can be investigated. Both cameras ⑩ (Fastcam SA5 CMOS cameras by Photron) are equipped with a 100 mm focal length lens ⑪ connected via a Scheimpflug adapter ⑫ to compensate for the oblique viewing angle  $\theta \approx 45^\circ$ . The Scheimpflug angle  $\gamma$  subtended by lens and image plane is adjusted to meet the Scheimpflug criterion.

Silicon oil particles with a mean diameter of  $d = 1 \mu\text{m}$  are seeded in both hot gas and coolant channel illuminating cropped camera frames with a resolution of each  $1.024 \text{ px} \times 512 \text{ px}$ . The double images are acquired at

Table 1. Operating parameters of the test section.

Parameter	Variable	Value
Reynolds number hot gas	$Re_{D,h}$	$13 \times 10^3$
Reynolds number coolant	$Re_{D,cc}$	$5 \times 10^3$
Density ratio	$DR$	1.7
Turbulence intensity hot gas	$Tu_h$	8.2%
Blowing ratio, (Equivalent $BR$ )	$BR$	0.5...1.5, (0.38...1.14)
Channel to main stream velocity ratio	$u_{cc}/u_h$	$\approx 0.15$
Total temperature hot gas	$T_{t,h}$	510 K
Total temperature coolant	$T_{t,c}$	300 K
Turbulent length scale	$l_e$	$0.73D$
Boundary layer displacement thickness	$\delta_1$	$0.05D$

a frequency of  $f = 2$  kHz in frame-straddling mode with a time delay of  $\Delta t = 30 \mu\text{s}$  at multiple lateral  $y/D$  positions. For camera and laser synchronization, a synchronizer by *iLA5150 GmbH* is used. For data evaluation, a multi-pass scheme with an overlap of 50% and a final interrogation window size of 16 px was used during evaluation with *PIVview3C* by *PIVTEC GmbH*, yielding approximately one velocity vector per millimetre.

Two geometries are investigated and detailed in Figure 2. The first geometry (Figure 2a) constitutes a  $10^\circ$ - $10^\circ$ - $10^\circ$  laidback fan-shaped (LFH) hole with a cylindrical inlet segment. The cylindrical part of the cooling holes is scaled up by a factor of  $\approx 14$  to a diameter of  $D = 10$  mm to facilitate a high spatial measurement resolution. Its length-to-diameter ratio is  $L/D = 7.5$ , the area ratio  $AR = A_{\text{outlet}}/A_{\text{inlet}} = 3.71$ , and the coverage ratio (hole breakout width based on the pitch) is 0.93. The edges of the diffuser are rounded with  $r_{\text{edge}} = 0.5D$  while inlet and breakout edges of the diffuser are sharp-edged. The ejection module contains a total of five LFH geometries with a pitch-to-diameter ratio of  $p/D = 3$  and an inclination angle of  $35^\circ$ . The coolant cross-flow is parallel to and in the same direction as the hot gas main stream flow. The second geometry is a slot geometry displayed in Figure 2b with an inclination angle and length-to-diameter ratio equivalent to that of the LFH geometry, where  $D$  is the diameter of the cylindrical part of the laidback fan-shaped geometry. The slot is  $b_{\text{slot}}/D = 0.4$  thick with edges rounded with  $0.4D$  at a spacing of  $p/D = 5.45$ , resulting in a coverage ratio of 0.8. In total, the ejection module contains three slot geometries. On the coolant side, a plenum-like structure is added, and the coolant cross-flow is opposite to that in the measurements of the laidback fan-shaped geometry.

A strong interaction between the individual film cooling jets can be expected for the LFH geometry due to their lateral proximity (Baldauf, 2001) and can be anticipated for the slot geometry as well.

## Measurement uncertainties

Detailed information regarding the measurement uncertainties of the flow parameters for both hot gas and coolant channel can be found in (Fraas et al., 2017). The measurement uncertainty, calculated according to (Kline, 1953), is below 12% for the heat transfer coefficient with film cooling  $h_f$  in all regions where the adiabatic cooling effectiveness  $\eta_{a,W} \leq 0.7$ . The uncertainty for the adiabatic film cooling effectiveness  $\eta_{a,W}$  is globally  $\leq 0.012$ .

For estimating the measurement uncertainty in the PIV experiments, a method based on correlation statistics (Wieneke, 2015) was used. In terms of absolute velocity, the spatially averaged relative local uncertainty was below 2.2%. The local relative uncertainty was found to be below 5% everywhere except in the close-wall region  $y/D < 0.4$  after which the local relative uncertainty increased locally towards the wall reaching up to 10%. Additionally, a slight decrease of uncertainty in streamwise direction of less than 1% was found.

## Results and discussion

In the following sections the geometries depicted in Figure 2 are analysed with regard to their aerothermal characteristics. For film cooling in gas turbines the most important aspects are the adiabatic film cooling effectiveness, the change in heat transfer due to film cooling and the potentially adverse or beneficial influence of the coolant ejection on the hot gas main flow and therefore the turbine blade aerodynamics. The latter affects the overall performance of a turbine blade and is often assessed globally (Ligrani, 2012; Lanzillotta et al., 2017) rather than for individual film cooling hole geometries. This can be attributed also to a lack of detailed aerodynamic investigations of film cooling hole geometries at realistic boundary conditions.

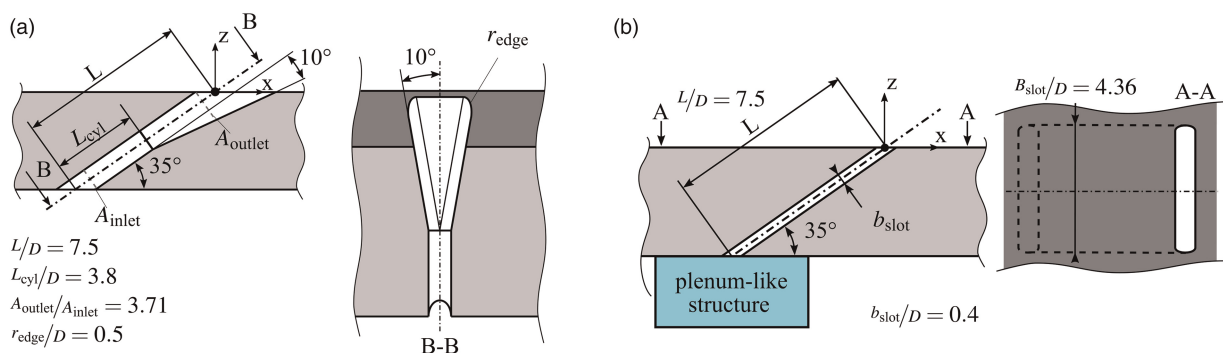


Figure 2. Film cooling hole geometries considered in the current study. (a)  $10^\circ$ - $10^\circ$ - $10^\circ$  laidback fan-shaped hole; (Fraas et al., 2019a). (b) Slot geometry with coolant side plenum-like structure.

For the following comparison of the geometries, it should be noted that the blowing ratio of the slot geometry was adapted in such a way, that an equal coolant mass flow per lateral length unit was achieved. So the mass flow ejected along  $y = 1D$  is equal for both the LFH10 and the slot geometry for corresponding blowing ratios. The corresponding blowing ratios are e.g.  $BR_{LFH10} = 0.5$  and  $BR_{slot} = 0.38$  and so on.

### Adiabatic film cooling effectiveness and heat transfer coefficient

In Figure 3 the spatial distribution of the adiabatic film cooling effectiveness  $\eta_{a,w}$  for both geometries is shown. For the LFH10, one can observe the expected trend of decreasing  $\eta_{a,w}$  along the streamwise direction  $x/D$  as well as from the streamwise centreline in both lateral directions  $\pm y/D$ . The peak adiabatic effectiveness is slightly asymmetric and shifted towards positive  $y/D$  values. An increase in blowing ratio generally increases  $\eta_{a,w}$  for the investigated blowing ratios but, as well known in literature, the current data also indicates a certain optimum, as the beneficial effect of an increase in blowing ratio  $BR$  reduces towards the highest blowing ratio  $BR$ . This can be observed much better in the laterally averaged adiabatic film cooling effectiveness  $\bar{\eta}_{a,w}$  in Figure 4a. The legend for Figure 4a is equivalent to that in Figure 4b.

For the slot, two lateral peaks in film cooling effectiveness can be observed for all blowing ratios. Towards higher blowing ratios and in streamwise direction  $x/D$  the double peak converges to a single maximum in lateral direction for each  $x/D$ . Directly downstream of the slot exit, the lateral extent of the film cooling imprint reduces for an increase in blowing ratio. This effect propagates and amplifies in streamwise direction, especially for the highest blowing ratio.

Comparing both geometries, much higher values of adiabatic cooling effectiveness  $\eta_{a,w}$  are evident for the slot and reflect strongly in the laterally averaged adiabatic cooling effectiveness  $\bar{\eta}_{a,w}$  as shown in Figure 4a along the streamwise direction  $x/D$ . Since the coolant mass flow per area is equivalent for both geometries, it can be

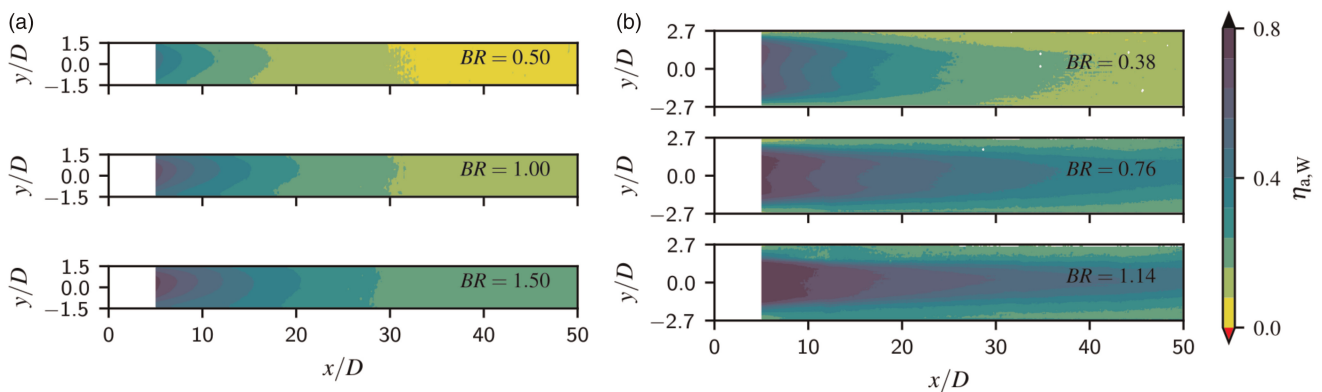


Figure 3. Spatial adiabatic film cooling effectiveness  $\eta_{a,w}$  for both geometries and three blowing ratios each. (a) LFH10,  $p/D = 3$ ,  $BR = 0.50, 1.00$  and  $1.50$ . (b) Slot,  $BR = 0.38, 0.76$  and  $1.14$ .

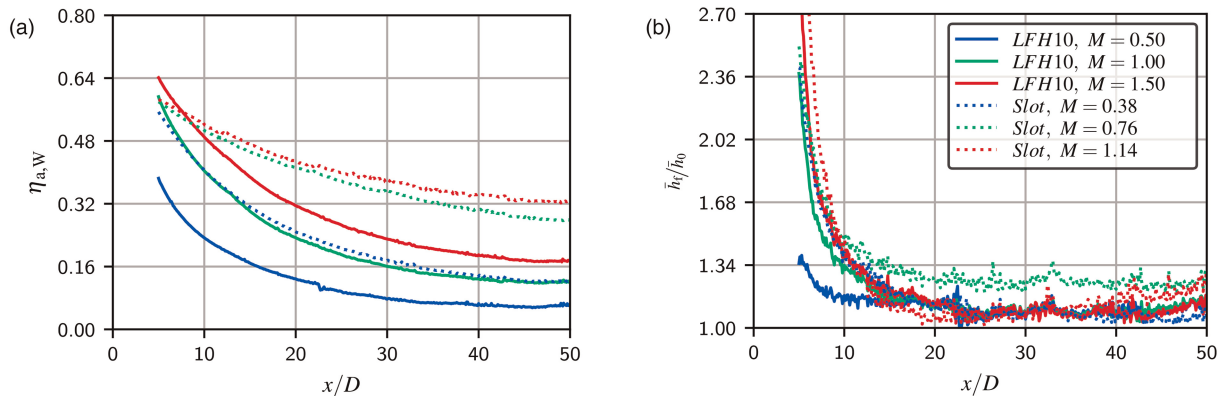


Figure 4. Laterally averaged adiabatic film cooling effectiveness  $\bar{\eta}_{a,w}$  (a) and ratio of heat transfer coefficients with and without film cooling  $h_f = h_o$  (b).

concluded that the coolant is used much more efficiently in case of the slot. For the investigated blowing ratios and geometries, an increase in  $\bar{\eta}_{a,W}$  for increasing blowing ratios is observed with a decrease in rate of change in  $\bar{\eta}_{a,W}$  towards the highest blowing ratio while the global maximum is achieved by the highest blowing ratio of the LFH10 geometry. However, for all blowing ratios the  $\bar{\eta}_{a,W}$  decays much more quickly for the LFH10 as compared to the slot geometry which can maintain relatively high values of  $\bar{\eta}_{a,W}$  along the entire investigated streamwise section. Only in case of the lowest blowing ratio of the slot geometry a nearly identical rate of change in streamwise direction is present.

Nearly no significant increase in  $\bar{\eta}_{a,W}$  can be achieved downstream of the slot cooling hole exit by increasing the blowing ratio from  $BR = 0.76$  to  $BR = 1.14$ . This is due to a potential coolant lift-off at this blowing ratio as will be discussed later in the flow field analysis. Further downstream, a more significant difference in  $\bar{\eta}_{a,W}$  can be observed, which can be attributed simply to the higher available coolant mass flow and the reattachment of parts of the coolant jet to the wall.

The laterally averaged ratio of heat transfer coefficients with and without film cooling  $h_f/h_0$  is displayed in Figure 4b and shows the expected behaviour for the LFH10: A decrease in  $h_f/h_0$  with decreasing blowing ratio and increasing streamwise position  $x/D$ . In case of the slot geometry,  $h_f/h_0$  also decreases with decreasing blowing ratio. For an increase in  $x/D$  the values of  $h_f/h_0$  do not follow a clear trend. For the lowest and highest blowing ratio, very similar  $h_f/h_0$  are observed at  $x/D = 12$  after which  $h_f/h_0$  for the highest blowing ratio drops below that of the lowest blowing ratio likely due to a coolant lift-off. The middle blowing ratio yields overall higher values of  $h_f/h_0$  compared to all other cases and maintains them at a relatively constant value for  $x/D \geq 18$ . Downstream of  $x/D = 25$   $h_f/h_0$  increases again for the highest blowing ratio and reaches the same level as that of the middle blowing ratio which indicates a reattachment of the coolant jet. For the slot geometry, this indicates that the coolant jet stays well-attached to the surface for the two lower blowing ratios. As long as the coolant film is attached, an increase in blowing ratio yields an increase in  $h_f/h_0$ . For the highest blowing ratio  $BR$ , the coolant film seems to get close to a detachment and the vortex structures of the jet in cross-flow have a less severe influence on the heat transfer coefficient. Comparing the LFH10 and slot geometry for the middle blowing ratio downstream of  $x/D = 20$  an average of  $\approx 25\%$  increase in  $h_f/h_0$  for the slot geometry is observed.

## Flow field analysis

While assumptions about the underlying aerodynamics of film cooling jets are often based on thermal film cooling parameters, measurements of the velocity field around the coolant-hot gas interaction are required to fully understand the competing effects causing the observations presented so far.

In Figure 5, velocity profiles normalised by the hot gas main flow velocity  $u_{ref}$  along the wall-normal direction are depicted for the absolute velocity  $u_{abs}$  and the velocity component in wall-normal direction  $w$  at the streamwise positions  $x/D = 0, 3, 6$  and  $9$  for central plane at  $y/D = 0$ . While the coolant mass flow per surface area is equivalent for respective blowing ratios in both geometries, the effective blowing ratio  $BR$  and momentum ratio  $IR$  are lower for the slot geometry. In case of the LFH10, these quantities are calculated for the cylindrical section of the cooling hole and depending on the diffusion achieved in the diffuser section of the hole a lower effective blowing ratio  $BR$  or momentum ratio  $IR$  is intended compared to the slot. The position of the LFH10 and slot exit geometries are indicated by the black lines below the  $x$ -axis with the line styles matching those in Figure 5 for the respective geometry.

For the absolute velocity in Figure 5a at  $x/D = 0$  very similar velocity profiles can be observed for all geometries and blowing ratios. The slot geometry leads to a slightly larger velocity gradient towards the wall and a slightly increased deceleration of the main flow for  $0.2 \leq z/D \leq 1.0$ . The wall-normal velocity component  $w$  at  $x/D = 0$ , shown in Figure 5b, increases with increasing blowing ratios for both geometries and is  $\neq 0$  even at  $y/D = 3$ . For LFH10 at the highest blowing ratio a near-wall regime with very high wall-normal velocities  $w$  can be observed. For the slot geometry, the overall wall-normal velocities are much larger compared to those of the LFH10 geometry at this streamwise position.

Further downstream at  $x/D = 3$  near-zero and negative wall-normal velocities can be observed in case of the slot, indicating the deflection of the coolant jet back towards the wall with increasing magnitude for increasing blowing ratios. In case of the LFH10, a further increase in wall-normal velocities can be observed at  $x/D = 3$  compared to the upstream position. Similarly as for the high blowing ratio at  $x/D = 0$ , the wall-normal velocity  $w$  peaks again towards the wall for the highest and even more so for the lowest blowing ratio. This indicates that the location, at which the coolant is ejected from the hole shifts depending on the blowing ratio due to a flow separation occurring in the laidback portion of the coolant hole. It partially blocks the coolant hole exit reducing

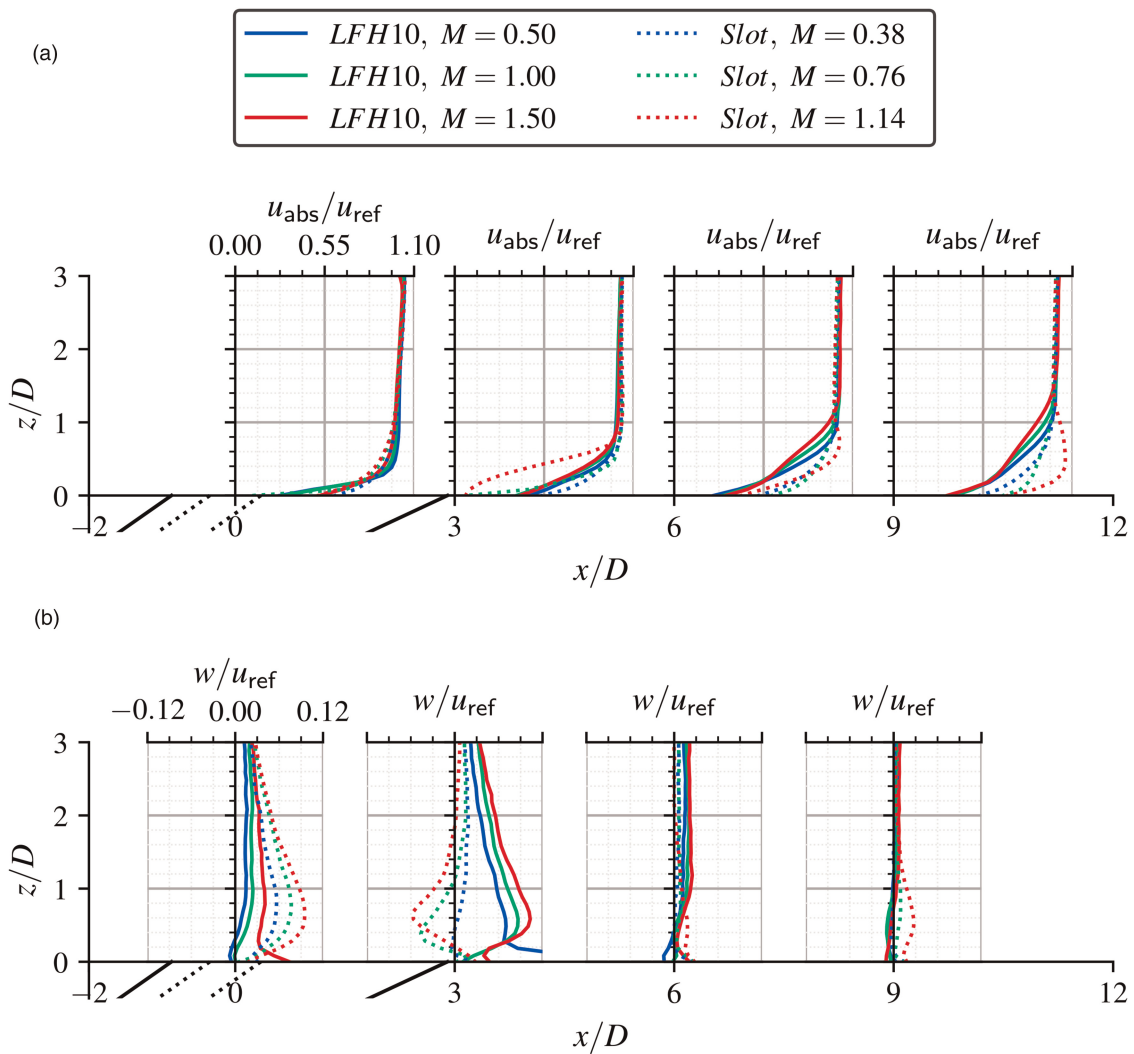


Figure 5. Normalised absolute and wall-normal velocities along wall normal direction for multiple  $x/D$  positions. Solid and dotted lines below the  $x$ -axes indicate the film cooling hole exits of the LFH10 and slot geometry, respectively. (a) Normalised velocity magnitude  $u_{abs}$  for  $x/D = 0, 3, 6$  and  $9$ . (b) Normalised wall-normal velocity  $w$  for  $x/D = 0, 3, 6$  and  $9$ .

the effective cross section and shifting the mean exit location of the coolant. Downstream of  $x/D \geq 6$  the wall-normal velocities for all cases are very uniform and approach zero at  $x/D = 9$  with only slight deviations in case of the slot geometry for  $BR = 1.14$ .

The absolute velocity profiles at  $x/D = 3$  for the LFH10 are still relatively similar for all blowing ratios, but the gradient is smaller compared to  $x/D = 0$ . For  $x/D = 6$  and  $9$  the differences with blowing ratio become more enhanced with decreasing velocities towards higher blowing ratios for  $0.2 \leq z/D \leq 1.2$ .

For the slot geometry a strong decrease in velocity towards increasing blowing ratios can be observed at  $x/D = 3$ , with the wall velocity gradient tending towards zero for  $BR = 1.14$ , potentially allowing a flow separation. At  $x/D = 6$  the coolant jet's wall-normal momentum is fully deflected in streamwise direction, so that the jet is attached to the wall producing near-wall velocity gradients  $\geq 0$  and a region with velocities higher than the reference velocity for  $0.5 \leq z/D \leq 1.0$ . Further downstream the velocity peak shifts towards the wall as seen for  $x/D = 9$ .

To understand the volumetric flow field, measurements were conducted at multiple lateral positions for the highest blowing ratio of each geometry by shifting the SPIV setup in Figure 1b in  $y$ -direction. This data was then interpolated laterally resulting in the velocity fields displayed in the  $y, z$ -plane in Figure 6 for  $x/D = 1$  and  $x/D = 9$ . The contour in the background encodes the absolute velocity  $u_{abs}$  and is overlaid by vectors showing the direction and magnitude of the in-plane components  $v$  and  $w$ . A reference vector indicating the correspondence between vector length and velocity is shown at the top right of each figure.

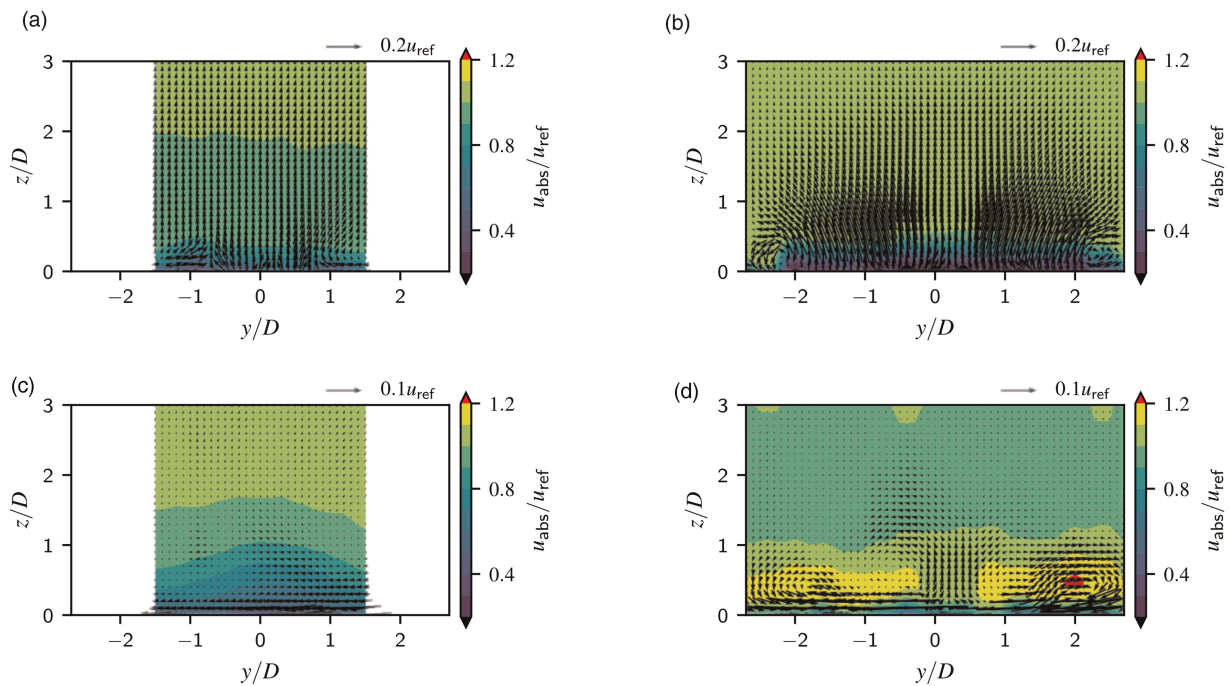


Figure 6. Velocity fields in the  $y, z$ -plane for the LFH10 geometry at  $BR = 1.50$  and the slot geometry at  $BR = 1.14$  for multiple  $x/D$  positions. (a) LFH10,  $\rho/D = 3$ ,  $x/D = 1$ . (b) Slot,  $x/D = 1$ . (c) LFH10,  $\rho/D = 3$ ,  $x/D = 9$ . (d) Slot,  $x/D = 9$ .

At  $x/D = 1$  (Figure 6a and b) the in-plane velocities are dominated by the wall-normal component  $w$  for both geometries which is expected as this streamwise position is within the hole breakout for both geometries. Nevertheless, secondary flow structures appear for both geometries mostly towards the lateral ends of the hole pitch. In both cases, the rotational direction corresponds to that expected for the two legs of the counter rotating vortex pair (CVP) which is found in many configurations of jets in cross-flow.

In generic jet in cross-flow (JIC) studies its origin is frequently associated with the effect of the jet's impulse on the cross-flow boundary layer, which would classify the CVP as a far-field phenomenon. Near-field studies indicate a different or at least additionally contributing formation process connected to a tilting and folding of the jet shear layer (Fric and Roshko, 1994; Karagozian, 2014). Numerical studies related to the JIC application in film cooling suggest a vortex pair formation already in the hole which at least contributes to the CVP (Baldauf and Scheurlen, 1996).

The position of the vortices for the current investigation suggest a formation outside the hole but very close to its exit in the near-field. For  $x/D = 9$  further downstream of the coolant ejection (Figure 6c and d), the in-plane velocities are distinctively different for both geometries. It has to be pointed out that the vector scaling is different in Figure 6a and b as compared to Figure 6c and d. In the first case, the unit vector at the top right of each figure represents a velocity magnitude of 20% of  $u_{ref}$ , whilst for the latter case it represents just 10% of  $u_{ref}$ , increasing the displayed length of each vector by a factor of two.

In case of the LFH10 geometry, no secondary motion related to the CVP can be observed at  $x/D = 9$ . Although not shown here, no secondary motions related to the CVP were found anywhere downstream of  $x/D \approx 1.5$ . The proximity of the neighbouring film cooling holes seems to suppress the CVP before it fully forms at all, which is expected and the intention for hole configurations with such a small pitch (Baldauf et al., 1999a,b).

For the slot geometry a complex vortex system can be observed at  $x/D = 9$ . The CVP-like vortex legs at the lateral ends at  $x/D = 1$  are now larger and have moved towards the centre by  $\approx 0.5D$ . The increase in wall-normal distance of the vortex cores to the wall in streamwise direction frequently observed for the CVP is nearly negligible. This supports the conclusions by Brittingham and Leylek (1997), who state that the lift typically produced by the two legs of the CVP is reduced by spreading them apart. An additional vortex pair with identical rotational direction can be observed closer to the centre of the jet. Both CVP-like vortex pairs suggest cross-flow entrainment in and below the coolant jet, which is typically associated with a reduction in adiabatic film cooling effectiveness and an increase in heat transfer coefficient. Obliterating the CVP is often the main goal of geometry studies. The current study, however, shows that amongst two geometries at comparable blowing ratios the one

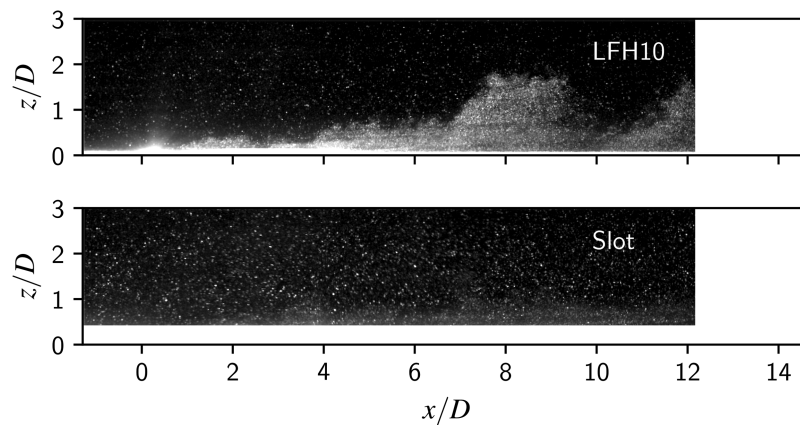


Figure 7. Dewarped instantaneous PIV raw images with enhanced coolant seeding for the streamwise, wall-normal centre plane; blowing ratio  $BR = 1.50$  for the LFH10 and blowing ratio  $BR = 1.14$  for the slot.

with the weaker CVP and lower momentum ratio  $IR$  is not necessarily achieving a lower  $\eta_{a,W}$ . Despite of the absence of the CVP and a theoretically lower momentum ratio for the LFH10, the adiabatic film cooling effectiveness is lower than that of the slot and also decreases much more quickly compared to the slot. Since the slot does show significant CVP-like vortex structures, it raises the question what else the effectiveness is influenced by to cause the observed results. For this purpose, a flow visualisation using enhanced PIV coolant seeding is used. In Figure 7, representative dewarped instantaneous PIV raw images are presented in the streamwise, wall-normal centre plane for the highest blowing ratio  $BR$  of both geometries. Brighter areas thereby correspond to coolant present in the flow. By “representative”, the authors refer to an instant in time, which shows a characteristic behaviour, which repeats itself at least qualitatively in many instants over the recorded time series.

In Figure 7, a clear qualitative difference between the coolant distribution for the different geometries can be observed. Coolant “chunks” are present for the LFH10 geometry, whose streamwise locations vary dependent on the chosen instant in time, whereas a uniform and relatively time-independent coolant distribution can be observed for the slot geometry. While both geometries are subjected to the same turbulent fluctuations in the main flow, the slot geometry seems to be much more robust towards local changes in the main flow velocity close to the hole exit. The instability of the exiting coolant for the LFH10 geometry is likely connected to a flow separation in the laidback section of the diffuser, which strongly responds to the instantaneous main flow boundary condition. The separation of these coolant “chunks” from the coolant jet into the main flow carries coolant away from the wall and effectively reduces the near-wall coolant mass flow drastically. It also indicates a flapping of the jet, which is responsible for creating the coolant “chunks” in the first place. Even if those merge back into the coolant jet again, their temperature would have increased due to the enhanced hot gas main flow exposure and mixing. This further detracts the cooling potential provided by a certain coolant mass flow. This also explains the more rapidly decreasing adiabatic film cooling effectiveness in case of the LFH10 geometry. The stability of the generated coolant jet or coolant film therefore plays an important role in how efficiently a provided coolant mass flow is used.

## Conclusion

In the current work two different geometries are analysed based on thermal as well as aerodynamic measurement data to emphasize the importance of a stable and continuous film cooling ejection on the resulting adiabatic film cooling effectiveness. Despite nearly completely suppressing the counter rotating vortex pair, the LFH10 compared to the slot geometry results in much lower laterally averaged adiabatic film cooling effectiveness  $\bar{\eta}_{a,W}$  due to non-stationary flow phenomena most likely occurring in the laidback section of the diffuser. The presented data clearly shows that the stability and continuity of the exiting coolant may be more important than obliterating the CVP. An improved understanding of film cooling and its wide range of influencing parameters should, therefore, be achieved based on analysing thermal film cooling quantities such as adiabatic film cooling effectiveness  $\eta_{a,W}$  and ratio of heat transfer coefficients with and without film cooling  $h_f/h_0$  combined with flow field information. Using techniques for flow field measurement constitutes an essential part of fully understanding which parameters to optimise for, especially at engine-realistic operating parameters.

## Nomenclature

---

### Latin symbols

$h_f, h_0$	heat transfer coefficient with and without film cooling ( $W/(m^2 K)$ )
$u, v, w$	velocity in streamwise, lateral and wall-normal direction (m/s)
$\dot{q}$	heat flux ( $W/m^2$ )
$D$	film cooling hole diameter (mm)
$L$	length (mm)
$P$	hole pitch (mm)
$T$	temperature (K)

### Greek symbols

$\eta_{a,W}$	adiabatic film cooling effectiveness (–)
$\delta$	boundary layer thickness (mm)
$\mu$	dynamic viscosity (kg s/m)
$\nu$	kinematic viscosity ( $m^2/s$ )
$\theta, \gamma$	camera angle, Scheimpflug angle ( $^\circ$ )

### Indices

$\square_{abs}$	absolute quantity
$\square_c$	referring to flow in cooling hole
$\square_{cc}$	referring to flow in the coolant channel
$\square_h$	referring to flow in hot gas channel
$\square_{ref}$	reference value
$\square_t$	total

### Abbreviations

FOV	field of view
IRT	infrared thermography
LFH	laidback fan-shaped hole
SPIV	stereoscopic Particle Image Velocimetry

### Acknowledgments

---

The investigations were conducted as part of the joint research program ECOFLEX-turbo in the frame of AG Turbo. The work was supported by the Federal Ministry for Economic Affairs and Climate Action (BMWK) as per resolution of the German Federal Parliament under grant number 03ET7091O. The authors gratefully acknowledge AG Turbo and Siemens Energy AG for the support.

### Funding sources

---

German Federal Ministry for Economics and Climate Action.  
Siemens Energy.

### Competing interests

---

Katharina Stichling declares that she has no conflict of interest. Hans-Jörg Bauer declares that he has no conflict of interest.

### References

---

Aga V. (2009). Experimental investigation of the influence of flow structure on compound angled film cooling performance. PhD thesis, ETH Zurich.

- auf dem Kampe T., Völker S., Sämel T., Heneka C., Ladisch H., et al. (2012). Experimental and numerical investigation of flow field and downstream surface temperatures of cylindrical and diffuser shaped film cooling holes. *Journal of Turbomachinery*. 135 (1): 011026. <https://asmedigitalcollection.asme.org/turbomachinery/article/135/1/011026/378450/Experimental-and-Numerical-Investigation-of-Flow>.
- Baldauf S. (2001). Filmkühlung thermisch höchstbelasteter Oberflächen: Korrelation thermographischer Messungen. PhD thesis, Logos-Verlag.
- Baldauf S. and Scheurlen M. (1996). CFD based sensitivity study of flow parameters for engine like film cooling conditions. In Volume 4: Heat Transfer; Electric Power; Industrial and Cogeneration, American Society of Mechanical Engineers.
- Baldauf S., Schulz A., and Wittig S. (1999a). High-resolution measurements of local effectiveness from discrete hole film cooling. *Journal of Turbomachinery*. 123 (4): 758–765. <https://doi.org/10.1115/1.1371778>
- Baldauf S., Schulz A., and Wittig S. (1999b). High-resolution measurements of local heat transfer coefficients from discrete hole film cooling. *Journal of Turbomachinery*. 123 (4): 749–757. <https://doi.org/10.1115/1.1387245>
- Brittingham R. A., and Leylek J. H. (1997). A detailed analysis of film cooling physics: Part IV— compound-angle injection with shaped holes. *Journal of Turbomachinery*. 122 (1): 133–145. <https://doi.org/10.1115/1.555419>
- Bunker R. S. (2005). A review of shaped hole turbine film-cooling technology. *Journal of Heat Transfer*. 127 (4): 441–453. <https://doi.org/10.1115/1.1860562>
- Choe H., Kays W., and Moffat R. (1974). The superposition approach to film-cooling, in American Society of Mechanical Engineers. In Winter Annual Meeting.
- Fraas M., Glasenapp T., Schulz A., and Bauer H.-J. (2017). Introducing a new test rig for film cooling measurements with realistic hole inflow conditions. In Volume 5C: Heat Transfer, American Society of Mechanical Engineers.
- Fraas M., Glasenapp T., Schulz A., and Bauer H.-J. (2019a). Film cooling measurements for a laidback fan-shaped hole: effect of coolant crossflow on cooling effectiveness and heat transfer. *Journal of Turbomachinery*. 141 (4): 041006. <https://doi.org/10.1115/1.4041655>
- Fraas M., Glasenapp T., Schulz A., and Bauer H.-J. (2019b). Optimized inlet geometry of a laidback fan-shaped film cooling hole – experimental study of film cooling performance. *International Journal of Heat and Mass Transfer*. 128: 980–990. <https://doi.org/10.1016/j.ijheatmasstransfer.2018.09.035>
- Fric T. F. and Roshko A. (1994). Vortical structure in the wake of a transverse jet. *Journal of Fluid Mechanics*. 279: 1–47. <https://doi.org/10.1017/S0022112094003800>
- Hale C. A., Plesniak M. W., and Ramadhyani S. (2000). Structural features and surface heat transfer associated with a row of short-hole jets in crossflow. *International Journal of Heat and Fluid Flow*. 21 (5): 542–553. [https://doi.org/10.1016/S0142-727X\(00\)00043-6](https://doi.org/10.1016/S0142-727X(00)00043-6)
- Johnson B., Tian W., Zhang K., and Hu H. (2014). An experimental study of density ratio effects on the film cooling injection from discrete holes by using PIV and PSP techniques. *International Journal of Heat and Mass Transfer*. 76: 337–349. <https://doi.org/10.1016/j.ijheatmasstransfer.2014.04.028>
- Karagozian A. R. (2014). The jet in crossflow. *Physics of Fluids*. 26 (10): 101303. <https://doi.org/10.1063/1.4895900>
- Kline S. J. (1953). Describing uncertainty in single sample experiments. *Mechanical Engineering*. 75: 3–8.
- Krein A. and Williams G. (2012). Flightpath 2050: Europe’s vision for aeronautics. In Innovation for Sustainable Aviation in a Global Environment: Proceedings of the Sixth European Aeronautics Days, Madrid. 30.
- Lanzillotta F., Sciacchitano A., and Rao A. G. (2017). Effect of film cooling on the aerodynamic performance of an airfoil. *International Journal of Heat and Fluid Flow*. 66: 108–120. <https://doi.org/10.1016/j.ijheatfluidflow.2017.05.011>
- Ligrani P. (2012). Aerodynamic losses in turbines with and without film cooling, as influenced by mainstream turbulence, surface roughness, airfoil shape, and mach number. *International Journal of Rotating Machinery*. 2012: 1–28. <https://doi.org/10.1155/2012/957421>
- Ochs M., Horbach T., Schulz A., Koch R., and Bauer H.-J. (2009). A novel calibration method for an infrared thermography system applied to heat transfer experiments. *Measurement Science and Technology*. 20 (7): 075103. <https://doi.org/10.1088/0957-0233/20/7/075103>
- Ochs M., Schulz A., and Bauer H.-J. (2010). High dynamic range infrared thermography by pixelwise radiometric self calibration. *Infrared Physics & Technology*. 53 (2): 112–119. <https://doi.org/10.1016/j.infrared.2009.10.002>
- Roach P. (1987). The generation of nearly isotropic turbulence by means of grids. *International Journal of Heat and Fluid Flow*. 8 (2): 82–92. [https://doi.org/10.1016/0142-727X\(87\)90001-4](https://doi.org/10.1016/0142-727X(87)90001-4)
- Schroeder R. P. and Thole K. A. (2016). Effect of high freestream turbulence on flowfields of shaped film cooling holes. *Journal of Turbomachinery*. 138 (9): 091001. <https://doi.org/10.1115/1.4032736>
- Stichling K., Elfner M., and Bauer H.-J. (2021). Investigation of film cooling using time-resolved stereo particle image velocimetry. *Journal of Turbomachinery*. 143 (7): 071014. <https://doi.org/10.1115/1.4050391>
- Wieneke B. (2015). PIV uncertainty quantification from correlation statistics. *Measurement Science and Technology*. 26 (7): 074002. <https://doi.org/10.1088/0957-0233/26/7/074002>
- Wright L. M., McClain S. T., and Clemenson M. D. (2011a). Effect of freestream turbulence intensity on film cooling jet structure and surface effectiveness using PIV and PSP. *Journal of Turbomachinery*. 133 (4): 041023.
- Wright L. M., McClain S. T., and Clemenson M. D. (2011b). PIV investigation of the effect of freestream turbulence intensity on film cooling from fanshaped holes. In Volume 5: Heat Transfer, Parts A and B, ASMEDC.